

The following resources related to this article are available online at www.sciencemag.org (this information is current as of December 5, 2009):

Updated information and services, including high-resolution figures, can be found in the online version of this article at:

<http://www.sciencemag.org/cgi/content/full/317/5837/490>

Supporting Online Material can be found at:

<http://www.sciencemag.org/cgi/content/full/317/5837/490/DC1>

A list of selected additional articles on the Science Web sites **related to this article** can be found at:

<http://www.sciencemag.org/cgi/content/full/317/5837/490#related-content>

This article **cites 15 articles**, 1 of which can be accessed for free:

<http://www.sciencemag.org/cgi/content/full/317/5837/490#otherarticles>

This article has been **cited by** 33 article(s) on the ISI Web of Science.

This article has been **cited by** 1 articles hosted by HighWire Press; see:

<http://www.sciencemag.org/cgi/content/full/317/5837/490#otherarticles>

This article appears in the following **subject collections**:

Materials Science

http://www.sciencemag.org/cgi/collection/mat_sci

Information about obtaining **reprints** of this article or about obtaining **permission to reproduce this article** in whole or in part can be found at:

<http://www.sciencemag.org/about/permissions.dtl>

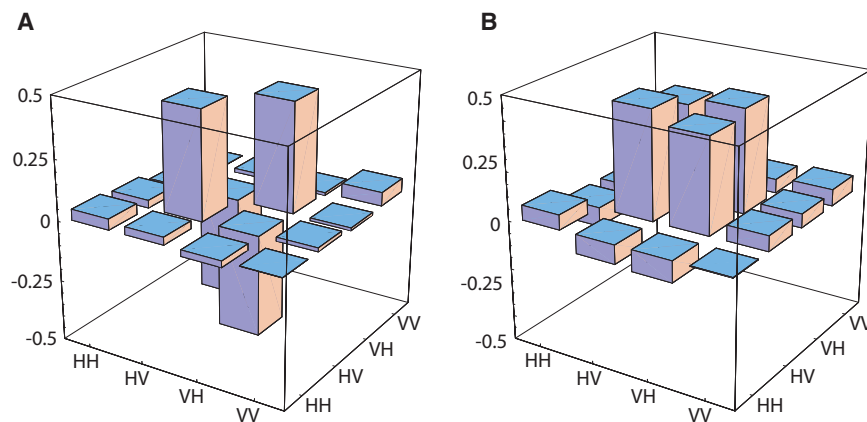


Fig. 4. Quantum state tomography. **(A)** Real part of the reconstructed density matrix for $B = 0$ and $t_S = 1.3 \mu\text{s}$. All imaginary parts (not shown) have a magnitude smaller than 0.03. Fidelity with the $|\Psi^-\rangle$ Bell state is 86.0(4)%. About 2200 entanglement events were collected for each of nine measurement settings. **(B)** For $B = -0.13 \text{ G}$ and $t_S = 2.8 \mu\text{s}$, the atomic superposition state rotates by π . The observed data correspond to a $|\Psi^+\rangle$ Bell state, with fidelity of 82.9(6)%. About 1800 entanglement events were obtained for each of six measurement settings. All imaginary parts (not shown) have a magnitude smaller than 0.05. In (A) and (B), equal detection efficiencies for all detectors were assumed.

tors (17). The resulting density matrix has only positive eigenvalues, and hence it represents a physically possible state. Its fidelity with respect to the expected Bell state, $|\Psi^-\rangle$ from Eq. 2, is $F = 86.0(4)\%$, with $0.5 < F \leq 1$ proving entanglement (18). From the density matrix, following (16), we derive a concurrence of $C = 0.73(7)$, with $0 < C \leq 1$ also proving entanglement. Because of technical imperfections, e.g., of polarizers in the detection setups, the observed fidelity/concurrence sets a lower bound for both the atom-photon and photon-photon entanglement achieved. The same measurements were done for $B = -0.13 \text{ G}$ and $t_S = 2.8 \mu\text{s}$ for which the atomic superposition state accumulates a π phase shift (compare to Fig. 3). Therefore, a density matrix corresponding to the Bell state $|\Psi^+\rangle \equiv \frac{1}{\sqrt{2}}(|+1, \sigma^-\rangle + |-1, \sigma^+\rangle)$ is expected. This is indeed observed (Fig. 4B) with a fidelity of $F = 82.9(6)\%$ and a concurrence of $C =$

$0.72(13)$. The state evolves between the two photon detections as a result of the constant magnetic field.

Future experiments could produce a time-independent $|\Psi^+\rangle$ Bell state by applying a pulsed magnetic field to the atom between entanglement generation and state mapping. Moreover, partial driving of the Raman transition in combination with atomic state manipulation should allow production of highly entangled multiphoton states (12). Our technique applied to a quasi-permanently trapped intracavity atom (3, 19) will push the probability of success even further, making the scheme truly deterministic. Two (or more) such systems operated in parallel are perfectly suited for teleportation and entanglement experiments in a quantum network (20–22) or quantum gate operations in a distributed and, hence, scalable quantum computer (23, 24).

References and Notes

1. E. Knill, R. Laflamme, G. J. Milburn, *Nature* **409**, 46 (2001).
2. A. Kuhn, M. Hennrich, G. Rempe, *Phys. Rev. Lett.* **89**, 067901 (2002).
3. J. McKeever *et al.*, *Science* **303**, 1992 (2004).
4. M. Keller, B. Lange, K. Hayasaka, W. Lange, H. Walther, *Nature* **431**, 1075 (2004).
5. M. Hijlkema *et al.*, *Nat. Phys.* **3**, 253 (2007).
6. T. Wilk, S. C. Webster, H. P. Specht, G. Rempe, A. Kuhn, *Phys. Rev. Lett.* **98**, 063601 (2007).
7. J. I. Cirac, P. Zoller, H. J. Kimble, H. Mabuchi, *Phys. Rev. Lett.* **78**, 3221 (1997).
8. H.-J. Briegel, W. Dür, J. I. Cirac, P. Zoller, *Phys. Rev. Lett.* **81**, 5932 (1998).
9. B. B. Blinov, D. L. Moehring, L.-M. Duan, C. Monroe, *Nature* **428**, 153 (2004).
10. B. Darquié *et al.*, *Science* **309**, 454 (2005).
11. J. Volz *et al.*, *Phys. Rev. Lett.* **96**, 030404 (2006).
12. C. Schön, E. Solano, F. Verstraete, J. I. Cirac, M. M. Wolf, *Phys. Rev. Lett.* **95**, 110503 (2005).
13. J. M. Raimond, M. Brune, S. Haroche, *Rev. Mod. Phys.* **73**, 565 (2001).
14. M. Hennrich, T. Legero, A. Kuhn, G. Rempe, *Phys. Rev. Lett.* **85**, 4872 (2000).
15. M. Hennrich, T. Legero, A. Kuhn, G. Rempe, *N.J. Phys.* **6**, 86 (2004).
16. D. F. V. James, P. G. Kwiat, W. J. Munro, A. G. White, *Phys. Rev. A* **64**, 052312 (2001).
17. J. B. Altepeter, E. R. Jeffrey, P. G. Kwiat, *Adv. At. Mol. Opt. Phys.* **52**, 105 (2005).
18. C. A. Sackett *et al.*, *Nature* **404**, 256 (2000).
19. S. Nußmann *et al.*, *Nat. Phys.* **1**, 122 (2005).
20. S. Bose, P. L. Knight, M. B. Plenio, V. Vedral, *Phys. Rev. Lett.* **83**, 5158 (1999).
21. L.-M. Duan, H. J. Kimble, *Phys. Rev. Lett.* **90**, 253601 (2003).
22. D. E. Browne, M. B. Plenio, S. F. Huelga, *Phys. Rev. Lett.* **91**, 067901 (2003).
23. Y. L. Lim, A. Beige, L. C. Kwek, *Phys. Rev. Lett.* **95**, 030505 (2005).
24. A. Serafini, S. Mancini, S. Bose, *Phys. Rev. Lett.* **96**, 010503 (2006).
25. We thank J. Bochmann and N. Kiesel for helpful discussions. This work was supported by the Deutsche Forschungsgemeinschaft [Collaborative Research Center 631, Research Unit 635, Munich Center for Advanced Photonics (MAP)] and the European Union [Information Society Technologies (SCALA) and Research Training Network (CONQUEST) programs].

16 April 2007; accepted 7 June 2007

Published online 21 June 2007;

10.1126/science.1143835

Include this information when citing this paper.

Porous Semiconducting Gels and Aerogels from Chalcogenide Clusters

Santanu Bag,^{1,2} Pantelis N. Trikalitis,^{2*} Peter J. Chupas,³ Gerasimos S. Armatas,^{1,2} Mercuri G. Kanatzidis^{1,2,4†}

Inorganic porous materials are being developed for use as molecular sieves, ion exchangers, and catalysts, but most are oxides. We show that various sulfide and selenide clusters, when bound to metal ions, yield gels having porous frameworks. These gels are transformed to aerogels after supercritical drying with carbon dioxide. The aerogels have high internal surface area (up to 327 square meters per gram) and broad pore size distribution, depending on the precursors used. The pores of these sulfide and selenide materials preferentially absorb heavy metals. These materials have narrow energy gaps (between 0.2 and 2.0 electron volts) and low densities, and they may be useful in optoelectronics, as photocatalysts, or in the removal of heavy metals from water.

Inorganic porous materials are at the foundation of broad applications such as molecular sieves, ion exchangers, and catalysts

(1, 2). Zeolites and aluminosilicate mesoporous materials constitute the vast majority of this class. Aerogels are another kind of porous inorganic

amorphous polymer in which nanosized blocks are interconnected to yield high internal surface area, very low densities, and large open pores (3, 4). Although the sol-gel chemistry of oxide-based materials (e.g., SiO_2 , Al_2O_3 , TiO_2) and carbon (5) is well known, successful attempts to apply this approach to non-oxide-based systems are quite rare, especially for chalcogenides. Such systems would be capable of combining the electronic properties of chalcogen-

¹Department of Chemistry, Northwestern University, Evanston, IL 60208, USA. ²Department of Chemistry, Michigan State University, East Lansing, MI 48824, USA. ³Advanced Photon Source, Argonne National Laboratory, Argonne, IL 60439, USA. ⁴Materials Science Division, Argonne National Laboratory, Argonne, IL 60439, USA.

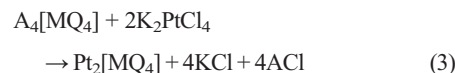
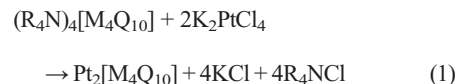
*Present address: Department of Chemistry, University of Crete, Heraklion 71409, Greece.

†To whom correspondence should be addressed. E-mail: m-kanatzidis@northwestern.edu

genides with internal porosity. Aerogels based on aggregated simple binary nanocrystals (e.g., CdS, CdSe) and on amorphous GeS₂ have been reported (6, 7).

We report on a strategy to create highly porous semiconducting aerogels derived from chalcogenide-based clusters and platinum as the linking metal ion (8). A family of chalcogenide

gels was prepared in aqueous solution with anionic [MQ₄]⁴⁻, [M₂Q₆]⁴⁻, and [M₄Q₁₀]⁴⁻ (M = Ge, Sn; Q = S, Se) building blocks (Fig. 1A) in the presence of platinum (II) salt, according to the following metathesis reactions:



where R = methyl, ethyl; M = Ge, Sn; Q = S, Se; and A = Na, K. In these reactions (e.g., Eq. 1), all chloride ligands of [PtCl₄]²⁻ can be replaced by the Q terminal atoms of chalcogenido clusters, generating materials with a formula of Pt₂[M₄Q₁₀]. Energy-dispersive spectroscopy (EDS) revealed that two platinum atoms per complex anion are incorporated in almost every case, giving a charge-balanced formula (Table 1). K⁺ or Cl⁻ ions, used as counterions in the synthesis, were not detected in the product—a result consistent with complete metathesis. This linking/polymerization reaction produced a continuous, extended Pt/M/Q framework of covalently bonded atoms that encapsulates solvent molecules into their pore system during the process of polymerization and finally makes hydrogels (fig. S1, A to C). Because the gels formed are based on all-chalcogenide species, we term these hydrogels “chalcogels” by analogy to the naming of cyanogels (9). Table 1 lists the six chalcogels we developed and the Zintl anion incorporated in each case.

After supercritical drying with CO₂, these chalcogels yield highly porous aerogels (Fig. 1, B and C) (10). All samples showed consistent Pt/M/Q (M = Ge, Sn; Q = S, Se) ratios very close to those in the starting clusters. However, slight discrepancies were observed for Chalcogel-3 and Chalcogel-6, which might be due to solution equilibrium processes.

Transmission electron microscopy (TEM) images of our aerogel samples revealed empty mesopores with no long-range order (Fig. 2, A to C). Indeed, they appear to be morphologically similar to the silica aerogels where particles are connected to each other, making continuous amorphous (Fig. 2D) networks. The micro- and mesoporosity were confirmed by nitrogen physisorption measurements. The adsorption-desorption isotherms show a type IV adsorption branch with a combination of H1- and H3-type hysteresis loops characteristic of an interconnected mesoporous system (Fig. 3) (11). This indicates that the mesopores have cylindrical and slit-shaped geometries. Pore size distribution plots calculated by the Barrett-Joyne-Halenda

Fig. 1. (A) Different building blocks used in chalcogel formation (blue spheres, metal centers; red spheres, chalcogenide atoms). (B and C) Monolithic hydrogel before (B) and after (C) supercritical drying, showing very little volume loss.

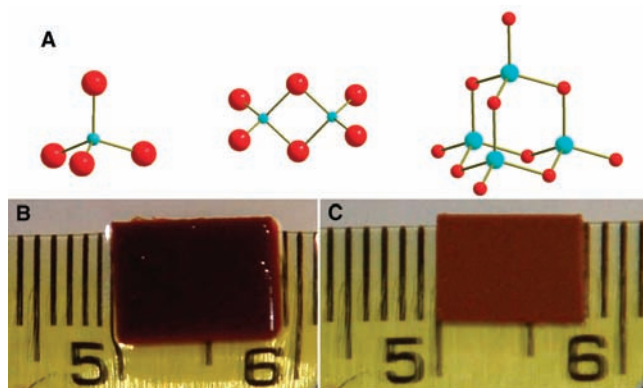


Table 1. Elemental analysis, colors, and optical energy gaps for the chalcogel series.

Chalcogel	Zintl anion	Pt/M/Q ratio*	Empirical formula	Color	Energy gap (eV)
Chalcogel-1	[Ge ₄ S ₁₀] ⁴⁻	2.0:4:9.6	Pt _{2.0} Ge ₄ S _{9.6}	Pinkish brown	2.0
Chalcogel-2	[Ge ₄ Se ₁₀] ⁴⁻	2.0:4:8.7	Pt _{2.0} Ge ₄ Se _{8.7}	Black	1.3
Chalcogel-3	[Sn ₄ Se ₁₀] ⁴⁻	2.1:4:9.7	Pt _{2.1} Sn ₄ Se _{9.7}	Black	1.0
Chalcogel-4	[Sn ₂ Se ₆] ⁴⁻	1.8:2:5.7	Pt _{1.8} Sn ₂ Se _{5.7}	Black	0.8
Chalcogel-5	[SnSe ₄] ⁴⁻	2.0:1:4.0	Pt _{2.0} SnSe _{4.0}	Black	0.2
Chalcogel-6	[SnS ₄] ⁴⁻	1.4:1:4.0	Pt _{1.4} SnS _{4.0}	Dark pinkish brown	1.4

*Based on EDS results. Listed values are an average of seven measurements on independently prepared samples.

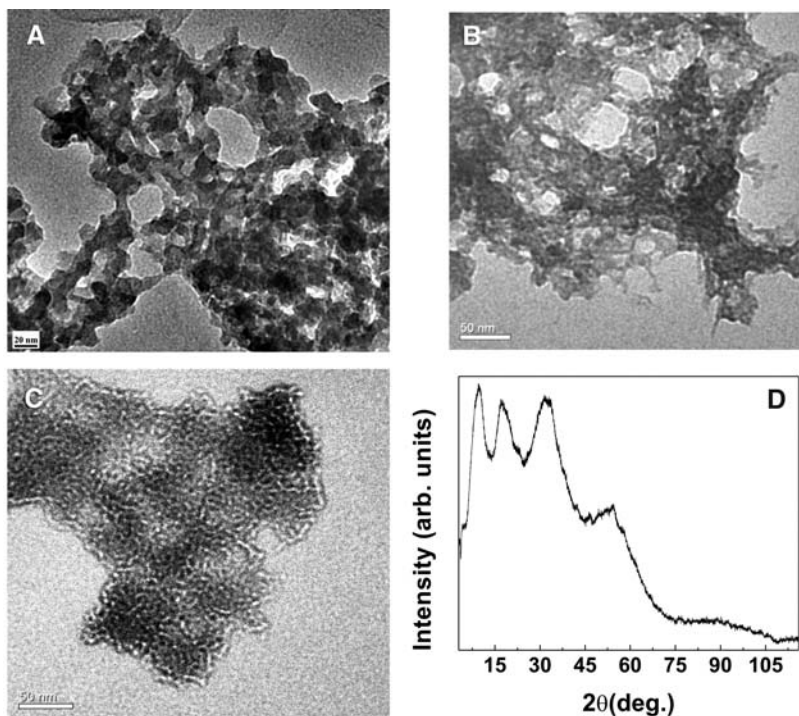


Fig. 2. (A and B) TEM images of Chalcogel-1 (A) and Chalcogel-2 (B). Pores between the particles in the meso- and macropore regime are clear from these pictures, although they are not ordered. (C) TEM image of Chalcogel-2 shows small pores inside the particle. Large macropores are absent here. (D) Wide-angle powder x-ray diffraction data for Chalcogel-1. The amorphous nature of the aerogel and the lack of other crystalline phases are obvious.

(BJH) method (11) from the desorption branch suggest the presence of a broad range of pore sizes in the meso region (fig. S1, D and E). Additionally, the absence of saturation in the adsorption isotherm implies the simultaneous presence of macropores (pore diameter >50 nm) in the samples, which would be consistent with the aerogel nature of these chalcogenides.

Brunauer-Emmett-Teller (BET) surface areas obtained from the aerogels range from 108 to 327 m²/g, depending on the chalcogenido cluster (Table 2). The surface area of 327 m²/g obtained from [Ge₄Se₁₀]⁴⁻ in Chalcogel-2 is the highest of the six chalcogels, followed by 323 m²/g for [Ge₄S₁₀]⁴⁻ in Chalcogel-1. The smallest cluster, [SnS₄]⁴⁻ in Chalcogel-6, gave the lowest BET surface area value of 117 m²/g. Given that the formula weights of these chalcogels are high, on a per-mole basis the surface area values are actually very large. The silica equivalence (12) BET surface area of Chalcogel-2 is 1674 m²/g and that of Chalcogel-3 is 1580 m²/g (Table 2). Values for silica aerogels range from 100 to 1600 m²/g and typical values are 600 m²/g. The bulk density of these chalcogels is very low; for example, Chalcogel-1 showed 0.12 to 0.17 g/cm³ with a skeletal density of 3.1 g/cm³.

To probe the local structure of the amorphous aerogels, we used the atomic pair distribution function (PDF) (13) technique, which analyzes both diffuse and Bragg scattering by recovering atom-atom correlations in real space in the form of a radial distribution function. A single correlation occurring at 2.36 Å is evident in the PDF of Chalcogel-1 (Fig. 4A), corresponding to the first-neighbor Ge-S and Pt-S bond distances. A clustering of correlations is evident around 3.52 Å, which corresponds to the second-neighbor Ge··Ge, S··S, and Pt··Ge distances. The PDF of Chalcogel-2 is remarkably similar to that of Chalcogel-1, although it exhibits a shift in correlations to longer interatomic distances *r* as a result of the larger atomic radius of Se versus S. Again a single correlation is evident in the PDF of Chalcogel-2 at 2.49 Å (Ge-Se and Pt-Se bond distances), and several appear centered around 3.75 Å. The higher intensity of the first correlation in Chalcogel-2 arises from the larger scattering factor of Se over that of S. Both PDFs show a lack of well-defined features past 6 Å that suggests a lack of long-range translational symmetry. However, a well-defined local structure is evident from the PDF and clearly shows that the adamantane clusters remain intact. The splitting of the correlations (3.52 Å and 3.75 Å) is likely due to subtle distortions, arising from linking of the adamantane clusters, that ultimately disrupt the long-range translational symmetry. The PDF data, together with the complete metathesis chemistry, elemental analysis, and x-ray photoelectron spectroscopy (XPS) (fig. S2), suggest a nonperiodic structure of the type shown in Fig. 4B. Further support for the integrity of the starting clusters in the final aerogels was provided by nuclear magnetic resonance (NMR)

(fig. S3), electrospray ionization mass spectroscopy (ESI-MS) (fig. S4), and infrared spectroscopy (fig. S5).

The chalcogels showed a remarkably high capacity for removing heavy metals from contaminated water. For example, starting with water

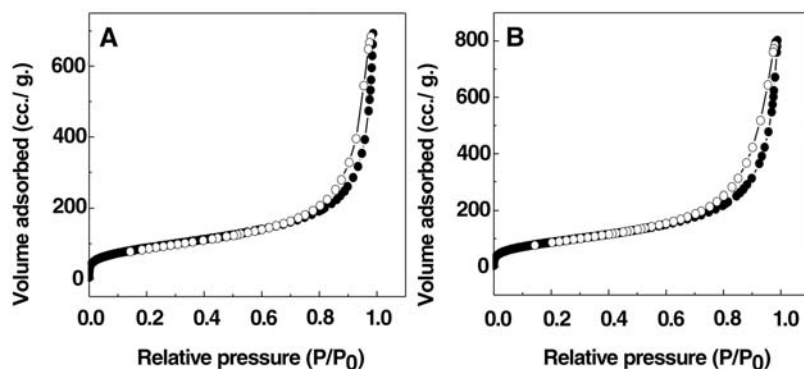


Fig. 3. Nitrogen adsorption-desorption isotherms of (A) Chalcogel-1 and (B) Chalcogel-2 at 77 K (solid circles, adsorption data; open circles, desorption data). Samples were degassed overnight at 348 K before testing.

Table 2. Nitrogen adsorption-desorption data for the chalcogel series.

Chalcogel	BET surface area (m ² /g)*	Surface area, silica equivalence (m ² /g)	Adsorption total pore volume (cm ³ /g)†
Chalcogel-1	276 to 323	1012 to 1184	0.59 to 0.73
Chalcogel-2	282 to 327	1444 to 1674	0.64 to 0.85
Chalcogel-3	196 to 271	1143 to 1580	0.52 to 0.70
Chalcogel-4	225 to 229	1296 to 1319	0.48 to 0.52
Chalcogel-5	210 to 211	1441 to 1448	0.44 to 0.48
Chalcogel-6	108 to 117	467 to 506	0.21 to 0.23

*Three independently prepared samples were measured.

†Single-point adsorption total pore volume was calculated at relative pressure (*P/P*₀) of 0.97.

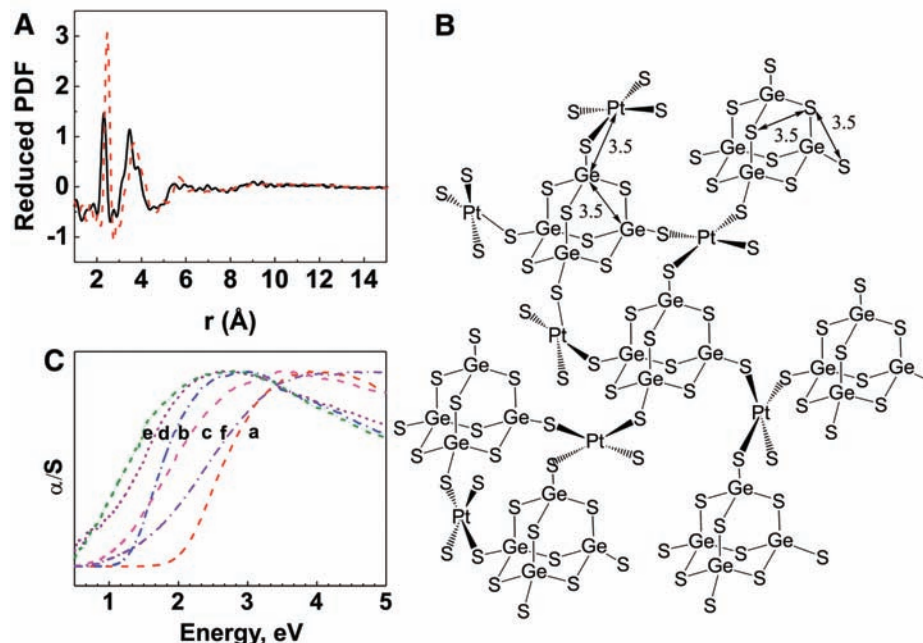


Fig. 4. (A) Reduced atomic pair distribution function $G(r)$ of Chalcogel-1 (black line) and Chalcogel-2 (red dashed line) as a function of interatomic distance *r*. (B) Interatomic distances (in angstroms) are shown for the [Ge₄S₁₀]⁴⁻ cluster in the proposed Chalcogel-1 structure. (C) Ultraviolet-visible electronic absorption spectra of (a) Chalcogel-1 (red dashed line), (b) Chalcogel-2 (blue dash-dot line), (c) Chalcogel-3 (magenta dashed line), (d) Chalcogel-4 (purple dotted line), (e) Chalcogel-5 (green dashed line), and (f) Chalcogel-6 (violet dash-dot line).

contaminated by 645 parts per million (ppm) Hg^{2+} , 10 mg of Chalcogel-1 removed Hg^{2+} down to concentration levels of ~ 0.04 ppm (14). Whereas mesoporous silicates need to be functionalized with surface-modified thiolate ligands before application toward environmental remediation (15), the chalcogels work directly as potential adsorbents for Hg^{2+} (16) without prior modification of their surface. The detailed mechanism of metal ion removal is not known.

The chalcogels also efficiently absorb organic hydrophobic aromatic molecules from solution. In contrast to the unmodified silica aerogels—which generally have hydrophilic surfaces and tend to be unstable under a humid atmosphere—the chalcogels present hydrophobic surfaces lined with chalcogen atoms and are immune to high humidity (17). Thermal gravimetric analysis indicates that the aerogels are stable to 180°C (fig. S6). As a demonstration of its high affinity for hydrophobic species, Chalcogel-1 absorbed quantitatively all of porphyrin I from a 5.67 $\mu\text{mol/liter}$ ethanolic solution within 24 hours (30 mg of Chalcogel-1 was shaken continuously in 16 ml of the porphyrin solution).

The chalcogels absorb light in the visible and infrared regions, exhibiting sharp energy gaps from 2.0 eV to 0.8 eV (Table 1) as determined by diffuse-reflectance solid-state ultraviolet-visible/near-infrared spectroscopy (Fig. 4C). Only Chalcogel-5 gave a broad absorption with a band gap of 0.2 eV. The optical properties of the highly porous semiconducting aerogels can be tuned by changing the building block. Going from the S to the Se analogs of the adamantane cluster, the energy gap decreases as expected. Also, by changing the group IV metal in the cluster from Ge to Sn, the energy gap is decreased by 0.3 eV. Similarly,

the band gap can also be changed by varying the chalcogenide content per metal in the starting clusters. This is well reflected in the observed band gaps of Chalcogel-3, -4, and -5, where the Se content per Sn atom is increased gradually and shows a narrowing of the energy gap.

Given that it is difficult to remove surfactants from mesostructured chalcogenide materials (18–22), the strategy reported here represents a convenient and general route for making porous materials with chalcogenide-based clusters. Because of the availability of a large number of soluble chalcogenido clusters, together with various linking transition and main-group metal ions, our approach seems to offer a general technique for preparing broad classes of porous chalcogenides.

References and Notes

- X. He, D. Antonelli, *Angew. Chem. Int. Ed.* **41**, 214 (2002).
- M. A. Carreon, V. V. Gulians, *Eur. J. Inorg. Chem.* **2005**, 27 (2005).
- C. J. Brinker, G. W. Scherer, *The Physics and Chemistry of Sol-Gel Processing* (Academic Press, San Diego, CA, 1990).
- N. Hüsing, U. Schubert, *Angew. Chem. Int. Ed.* **37**, 22 (1998).
- R. W. Pekala, C. T. Alviso, F. M. Kong, S. S. Hulsey, *J. Non-Cryst. Solids* **145**, 90 (1992).
- J. L. Mohanan, I. U. Arachchige, S. L. Brock, *Science* **307**, 397 (2005).
- K. K. Kalebaila, D. G. Georgiev, S. L. Brock, *J. Non-Cryst. Solids* **352**, 232 (2006).
- See supporting material on Science Online.
- M. Heibel, G. Kumar, C. Wyse, P. Bukovec, A. B. Bocarsly, *Chem. Mater.* **8**, 1504 (1996).
- S. S. Kistler, *J. Phys. Chem.* **36**, 52 (1932).
- S. J. Gregg, K. S. W. Sing, *Adsorption, Surface Area and Porosity* (Academic Press, New York, 1982).
- The molecular formulas were normalized to two sulfur or two selenium atoms to compare well with SiO_2 (e.g.,

- $\text{Pt}_2\text{Ge}_5\text{S}_{10}$ is converted to $\text{Pt}_{0.4}\text{Ge}_{0.8}\text{S}_2$ having formula weight of 220.27) for equivalent surface area calculation.
- S. J. L. Billinge, M. G. Kanatzidis, *Chem. Commun.* **2004**, 749 (2004).
 - The capacity of Chalcogel-1 to remove Hg^{2+} from aqueous solution is extremely high (645 mg/g or 3.21 mmol/g). This tremendous affinity is also reflected in the calculated distribution coefficient K_d^{Hg} [defined as the amount of adsorbed metal (in micrograms) on 1 g of adsorbing material divided by the metal concentration (in milligrams per milliliter) remaining in the treated water (8)]. K_d^{Hg} values varied from 0.92×10^7 ml/g (at 92 ppm Hg^{2+}) to 1.61×10^7 ml/g (at 645 ppm Hg^{2+}).
 - L. Mercier, T. J. Pinnavaia, *Adv. Mater.* **9**, 500 (1997).
 - The specific binding of chalcogels with heavy metals was demonstrated by adding 5 ml each of 89 ppm Zn^{2+} and 92 ppm Hg^{2+} solutions to 10 mg Chalcogel-2 and stirring for 24 hours at room temperature. The final solution contained 52.8 ppm Zn^{2+} and 0.1 ppm Hg^{2+} .
 - The BET surface area remained high after storing the chalcogels for longer times. For example, the surface area of Chalcogel-2 decreased from 327 to 303 m^2/g after 5 weeks and to 265 m^2/g after 3 months.
 - M. J. MacLachlan, N. Coombs, G. A. Ozin, *Nature* **397**, 681 (1999).
 - P. N. Trikalitis, K. K. Rangan, T. Bakas, M. G. Kanatzidis, *Nature* **410**, 671 (2001).
 - P. N. Trikalitis, K. K. Rangan, M. G. Kanatzidis, *J. Am. Chem. Soc.* **124**, 2604 (2002).
 - P. N. Trikalitis, K. K. Rangan, T. Bakas, M. G. Kanatzidis, *J. Am. Chem. Soc.* **124**, 12255 (2002).
 - S. D. Korlann, A. E. Riley, B. L. Kirsch, B. S. Mun, S. H. Tolbert, *J. Am. Chem. Soc.* **127**, 12516 (2005).
 - We thank T. J. Pinnavaia and D. Holmes for use of the nitrogen sorption measurement and NMR handling, respectively. Use of the Advanced Photon Source was supported by the U.S. Department of Energy, Office of Science, Office of Basic Energy Sciences.

Supporting Online Material

www.sciencemag.org/cgi/content/full/317/5837/490/DC1
Materials and Methods
Figs. S1 to S6
References

14 March 2007; accepted 5 June 2007
10.1126/science.1142535

Stabilization of Labile Carbonyl Addition Intermediates by a Synthetic Receptor

Tetsuo Iwasawa, Richard J. Hooley, Julius Rebek Jr.*

Products of unfavorable chemical equilibria are not readily observed because their high energy and increased reactivity result in low concentrations. Biological macromolecules use binding forces to access unfavorable equilibria and stabilize reactive intermediates by isolating them from the medium. In a similar vein, we describe here a synthetic receptor that allows direct observation of labile tetrahedral intermediates: hemiaminals formed in the reaction of an aldehyde carbonyl group with amines. The receptor encapsulates alkyl-substituted primary amines, then orients them toward a covalently tethered aldehyde function. The hemiaminal intermediates appear at high concentration, confined from the bulk solution and observable at ambient temperature by conventional nuclear magnetic resonance spectroscopy.

Chemical reactions often proceed through many intermediate stages between starting materials and products. The reactive intermediates at such stages are generally not observed directly, because their concen-

trations are vanishingly small, but are treated through steady-state approximations and detected by kinetic or other methods (1, 2). The reaction of carbonyl compounds with nucleophiles invariably involves an addition step that

gives an unstable tetrahedral carbon intermediate followed by an elimination step. For example, the reaction of primary amines with aldehydes to give imines (Fig. 1) proceeds through an intermediate hemiaminal (3). The process is catalyzed by acids or bases, and the proton transfers involved generate additional transient, charged intermediates. The hemiaminal is, except in very special cases (4–6), not observed. It is energetically disfavored, because the cost of breaking the carbonyl π bond and the entropic price of bringing the two reactants together are not compensated by the new covalent bonds formed. Accordingly, the unstable hemiaminal dissociates to starting materials or proceeds to imine with loss of water. We tailored a molecular receptor to favor formation of this intermediate and found that the hemiaminal was stabilized for minutes to hours, long

Skaggs Institute for Chemical Biology and Department of Chemistry, Scripps Research Institute, 10550 North Torrey Pines Road, La Jolla, CA 92037, USA.

*To whom correspondence should be addressed. E-mail: jrebek@scripps.edu